Retrieval of Cloud Properties and Aerosol Direct Radiative Forcing

CERES Science Team Meeting 23
Williamsburg, VA
23-26 January 2001

M.A. Friedman, W.R. Tahnk, and J.A. Coakley, Jr.

College of Oceanic and Atmospheric Science
Oregon State University
Corvallis, OR 97331-5509

1. Introduction

Work at Oregon State University focused on two problems: the retrieval of cloud properties from the VIRS imager and the determination of the aerosol direct radiative forcing based on CERES SSF Edition 1 data. With regard to the retrieval of cloud properties, special attention was focused on VIRS fields of view overcast by single-layered, opaque clouds in order to investigate further the discrepancies between droplet effective radii obtained with the CERES operational algorithm and those derived with an independent algorithm developed at OSU. Further work was also undertaken to develop a scheme for the retrieval of cloud properties from imager fields of view that are only partially cloud covered. With regard to the determination of the aerosol direct radiative forcing, TRMM CERES SSF observations were collocated with surface, AERONET observations of aerosol optical depth. The correlation of TOA fluxes with the AERONET optical depths leads to an empirical estimate of the aerosol, direct radiative forcing (Satheesh and Ramanathan 2000).

2. Retrieval of cloud properties

The first item addressed after the previous meeting was further investigation into a possible source for discrepancies in overcast cloud retrieval products obtained by OSU and NASA-Langley. Examples of optically thick overcast clouds were identified, and the observed 3.7-μm radiance was broken down into its various components. The examples were sent to NASA-Langley for direct comparison, and prompted the inclusion of N_2O in the NASA-Langley retrievals to match the OSU approach. The resulting comparisons of the twenty previously identified scenes showed significant improvement, with agreement in effective radius to within 2 μm in most cases. Nevertheless, several scenes still show anomalies in optical depth and cloud altitude. The twenty comparisons have been provided to D. Young of NASA-Langley to aid in clearing up the remaining problems.

Improvements to the partly cloudy retrieval algorithm have been made. Calculated cloud-free radiances at 0.63, 3.7, and 11 μm were replaced by mean observed cloud-free values for the analysis region. Differences in retrieved visible optical depth and droplet effective radius were greater than 1 and 1 μm, respectively, when the cloud fraction was less than approximately 20%. The quality of the partly cloudy retrievals was also improved by removing cases in which upper-level clouds were present. The primary effect of upper-level clouds was anomalously high cloud fractions, much greater than 100%.

Emission and surface reflectance at 3.7 μm were determined. Nighttime cloud-free ocean observations were plotted, and a fitted curve was calculated following the method of Coakley and Davies (1986). The fitted equation has the form

$$I_{3.7} = (8.67 \times 10^{-8}) I_{11}^{3.39}$$

The equation was then used to calculate the thermal contribution to the daytime 3.7-μm radiance, and subsequently, the 3.7-μm reflectance was derived. The derived 3.7-μm reflectances were very close to 0% with an uncertainty of about 2%. The fitted 11-μm and 3.7-μm emission was also compared to the calculated tropical (and midlatitude) emission used in the retrievals. While the tropical emission curves for nadir and limb views intersect most of the distribution of observed points, they do not match the slope of the fitted curve. Discrepancies between the calculated emission and the fitted emission (and observations) are on the order of 0.05 $mWm^{-2}sr^{-1}cm$. For overcast radiances, this uncertainty in 3.7-μm radiance would correspond to errors in effective radius of 1 to 2 μm for smaller droplets, and about 5 μm for droplets having effective radii greater than 20 μm.

Properties of clouds taken from overcast and partly cloudy pixels have been compared. In one of the cases studied (a 100-km × 100-km subregion of 980212 19:03), the distribution of cloud fraction for the partly cloudy pixels shows that most of the population has very high cloud fractions and that a secondary population has very small cloud fractions. When effective radius and optical depth are plotted as a function of cloud fraction, there is a distinct trend in effective radius towards higher values for higher cloud

fractions. Optical depth values are small and almost constant for partly cloudy pixels with cloud fractions between 20% and 80%. Also, optical depths of partly cloudy pixels approach optical depths of overcast pixels as cloud fraction increases over 80%. Cloud fractions of over 100% are possible since the mean overcast 11-μm cloud radiance for a larger region that surrounds the region being analyzed is used for I_c in the derivation of cloud fraction:

$$A_c = \frac{I - I_s}{I_c - I_s}.$$

I_s is the mean observed cloud-free 11-μm radiance for the region, and I is the observed 11-μm radiance for the pixel.

The distribution of retrieved optical depth and effective radius for overcast pixels, partly cloudy pixels, and partly cloudy pixels retrieved as if they were overcast were also compared for the subregion. Overcast pixels had the highest mean values for optical depth and effective radius. Retrieving partly cloudy pixels as if they were overcast produced lower mean retrieved optical depths and higher mean retrieved effective radii, relative to the optical depths and effective radii when allowance for the fractional cloud cover was included in the retrievals. The same relative distributions are seen in other examples for which the population of partly cloudy pixels is larger, such as 980222 15:41.

The sensitivity of the partly cloudy retrievals to uncertainties in surface radiances and cloud emission temperature is being investigated. Also, an automated scheme is being developed to screen cases with upper-level clouds. Further work will determine the

systematic differences in cloud properties retrieved for overcast and partly cloudy pixels, and the impact of these differences on radiative fluxes.

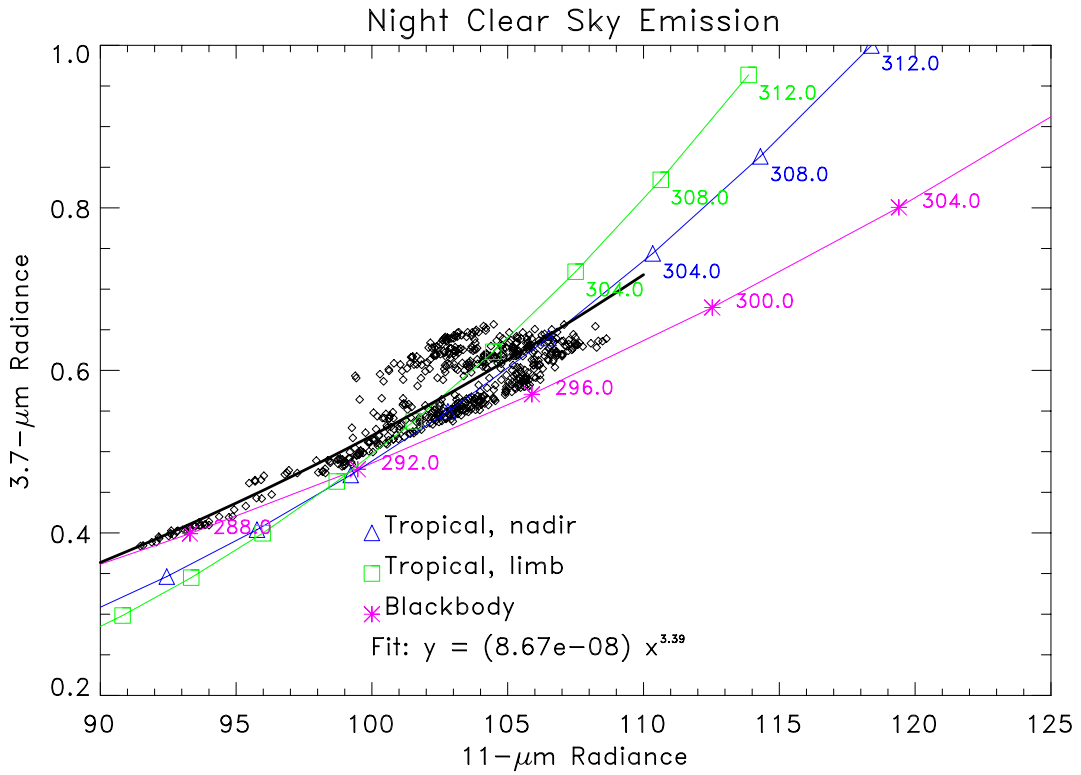

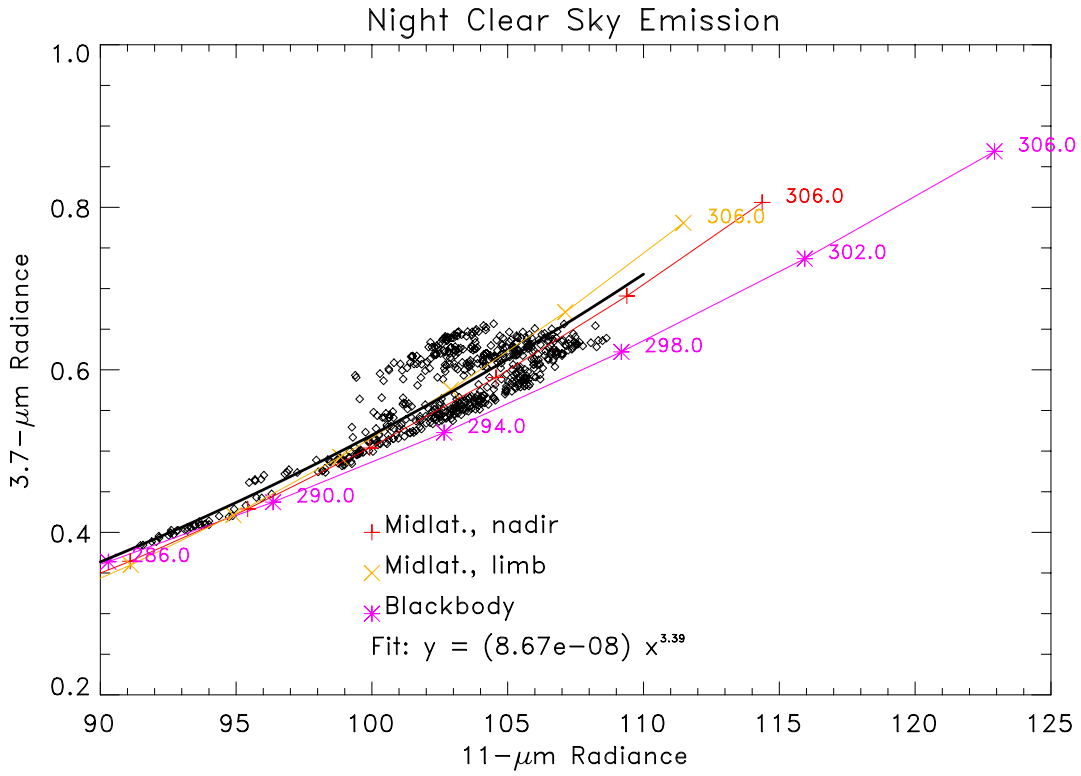

Thermal emission for averaged cloud-free nighttime observations. Differences between the fitted curve and the observed and calculated tropical (top) and midlatitude (bottom) emission used in the retrievals leads to differences in effective radius of several μm for overcast pixels.

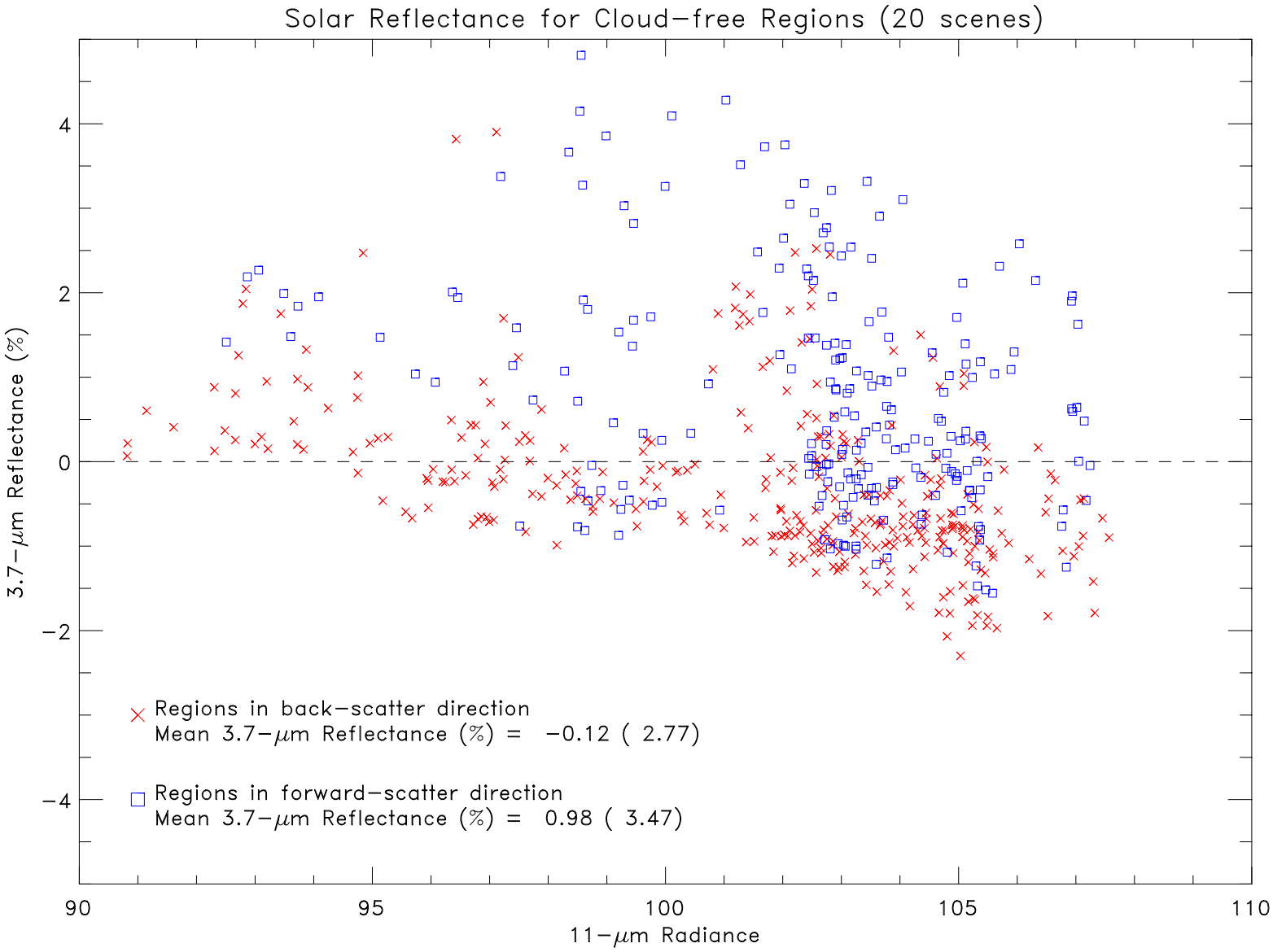

Derived cloud-free solar reflectance is shown for the twenty comparison scenes partitioned into back-scatter and forward-scatter directions. Reflectances are close to 0%, with an uncertainty of about 2%.

CALCULATED AND OBSERVED RADIANCES

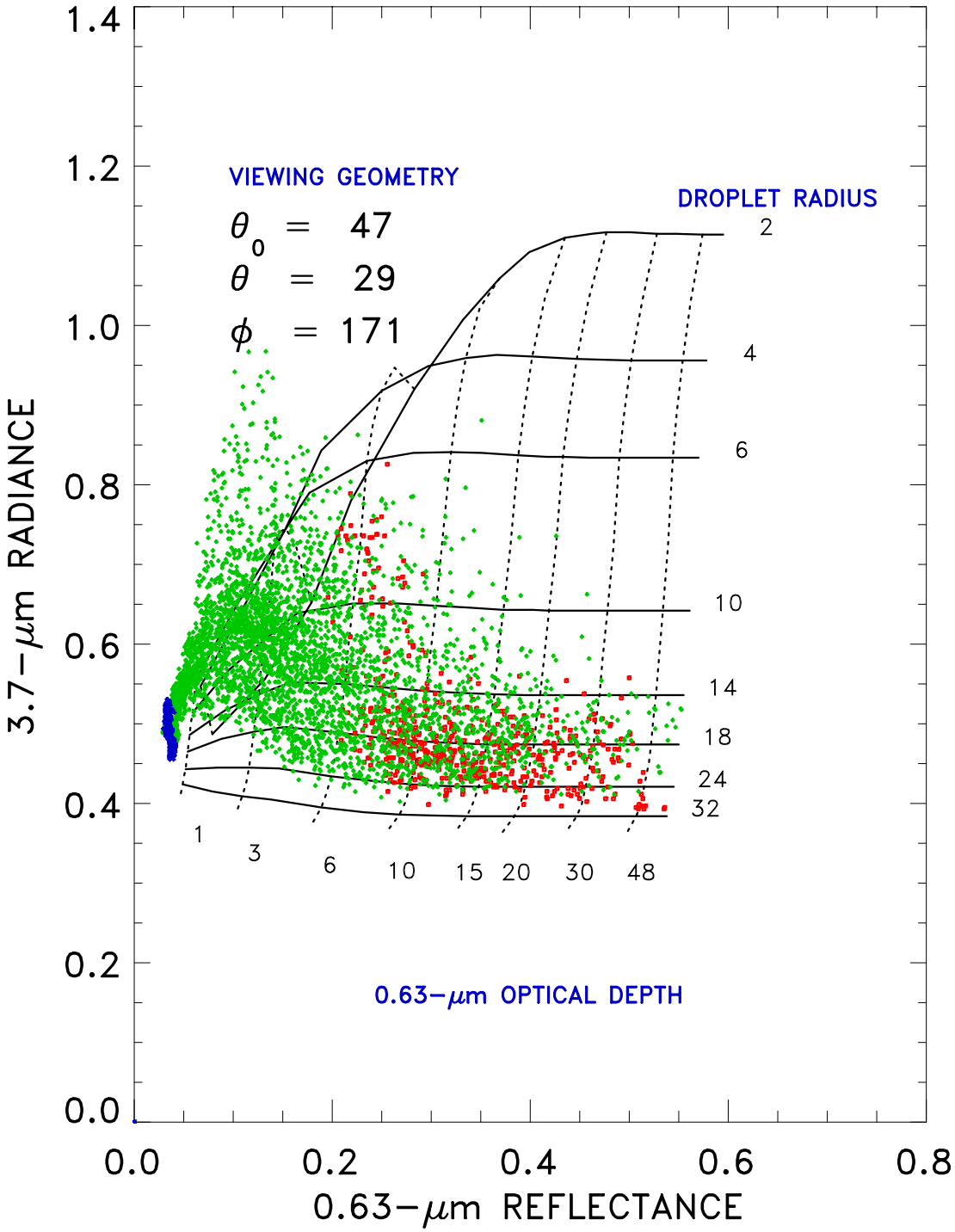

An uncertainty of 0.05 mWm^{-2} sr^{-1}cm for overcast radiances corresponds to errors in effective radius of 1 to 2 μm for smaller droplets, and about 5 μm for larger droplets. The observations are VIRS pixel radiances for a 100 × 100-km ocean region. Overcast pixels are denoted by red points, partly cloudy pixels by green points.

PARTLY CLOUDY RETRIEVAL PRODUCTS

980212 19:03

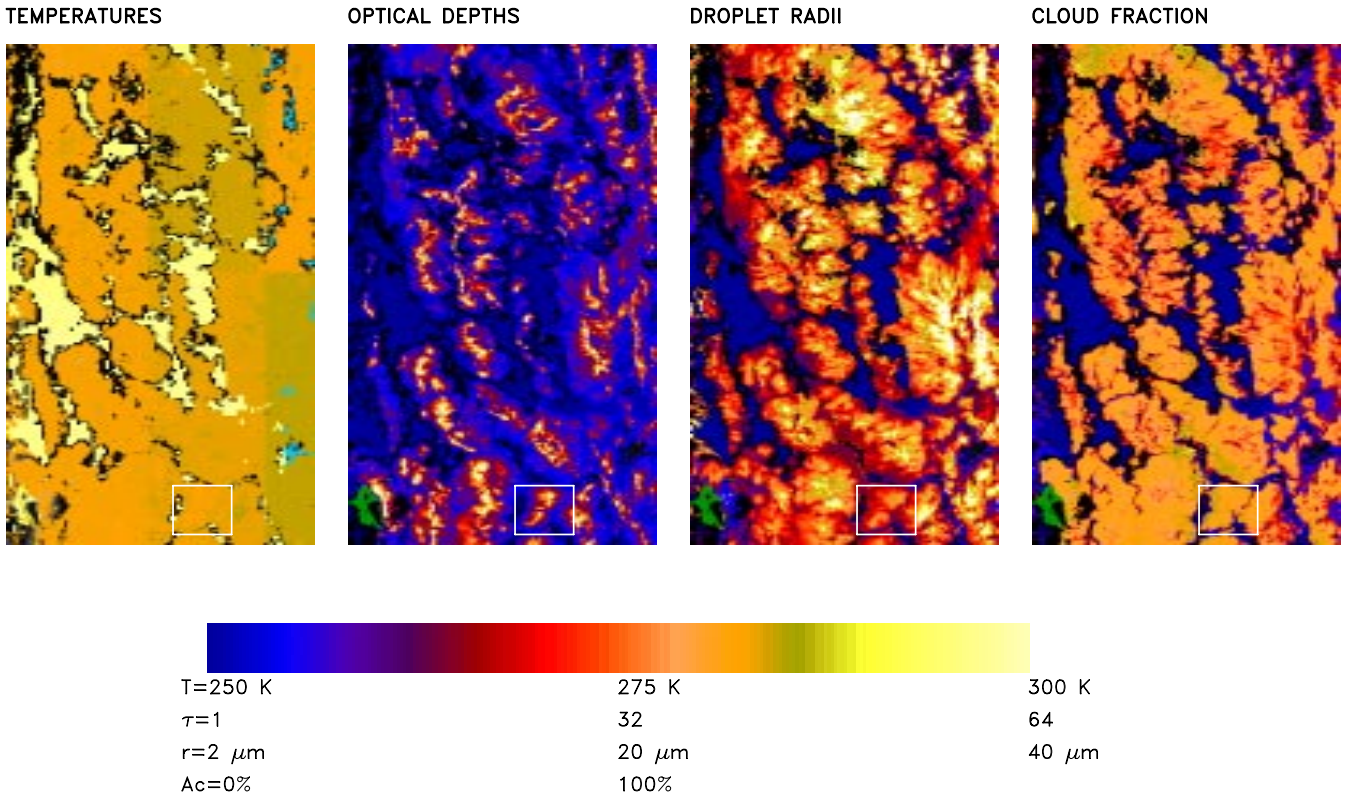

Cloud properties are shown for 980212 19:03. The light blue pixels in the leftmost panel represent cloud-free pixels that fall within the sun glint cone angle cutoff. The small subregion near the bottom of the panels is a 100 × 100-km region that is examined more closely in the following figures.

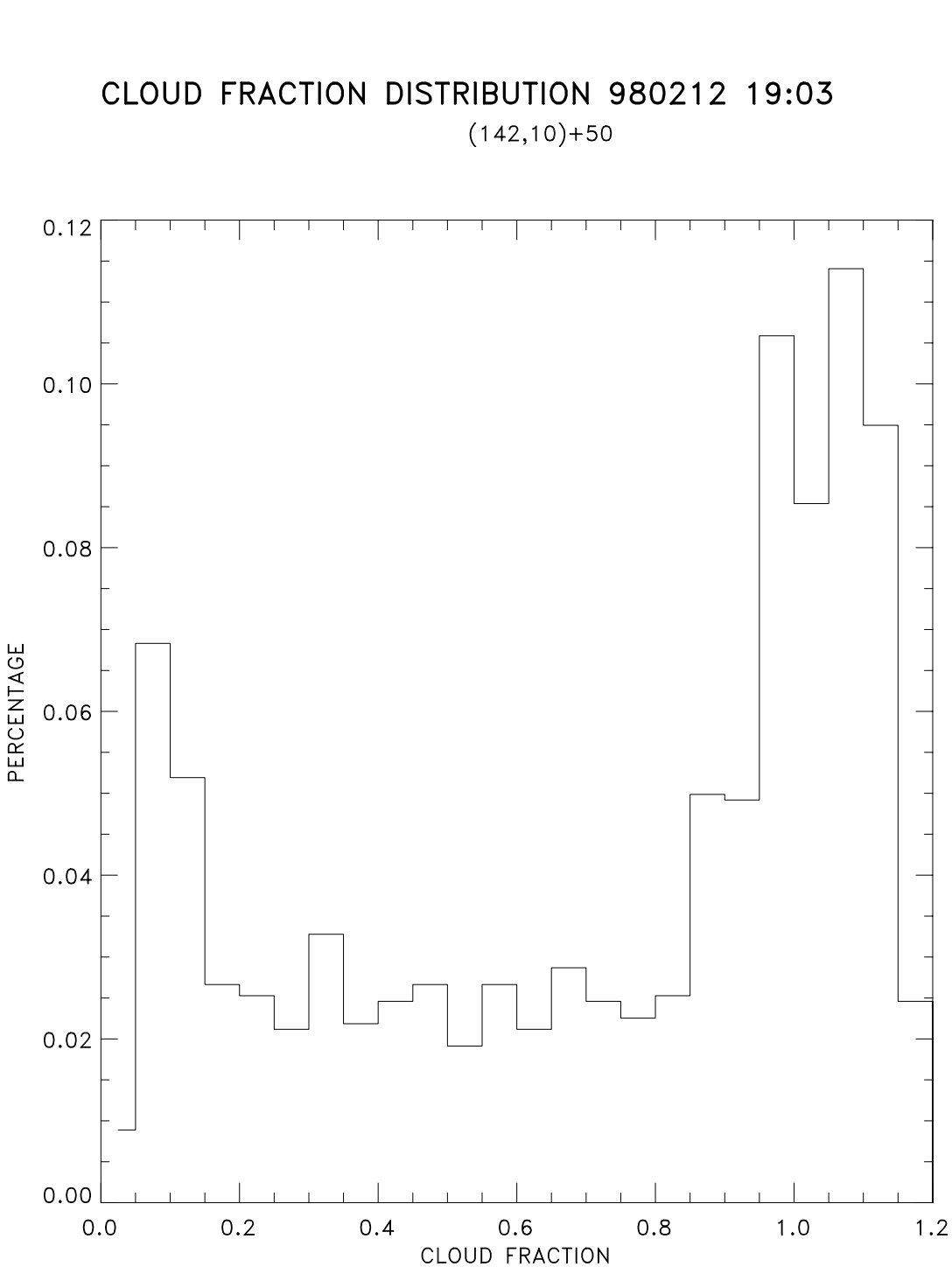

The distribution of cloud fraction is shown for the subregion of 980212 19:03 defined in the previous figure. The largest population occurs at very high cloud fractions, with a secondary population at very low cloud fractions. Cloud fractions can be greater than 1.0 because the mean overcast 11-μm radiance was taken from a larger region that surrounds the subregion.

PARTLY CLOUDY PROPERTIES 980212 19:03

Grid box (142,10), 50 x 50

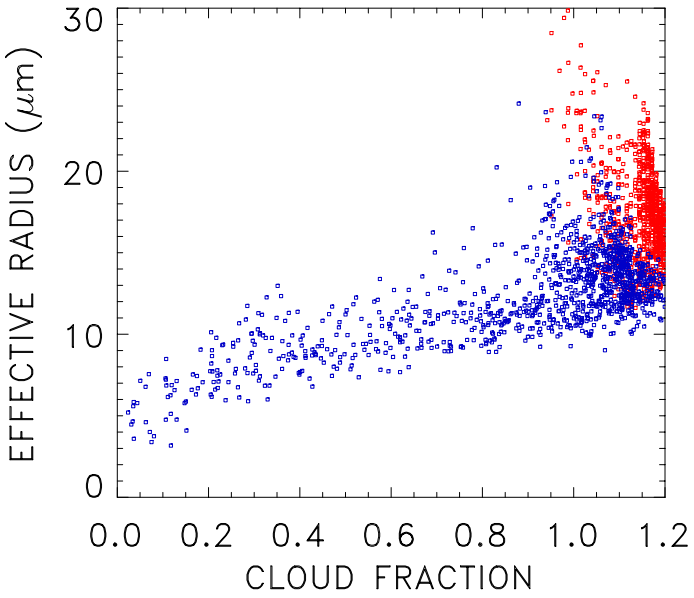

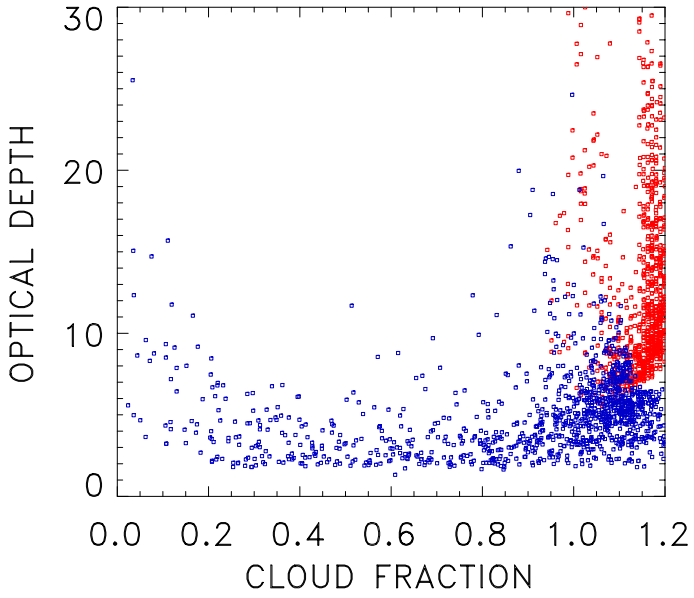

Partly cloudy effective radius and optical depth retrievals for the subregion are shown as a function of cloud fraction. Retrieved r_e increases with cloud fraction. Retrieved τ is fairly constant for $.2 < A_c < .8$, and approaches the wide range of overcast values for $A_c > .8$.

DISTRIBUTION COMPARISONS 980212 19:03

Grid box (142,10), 50 x 50

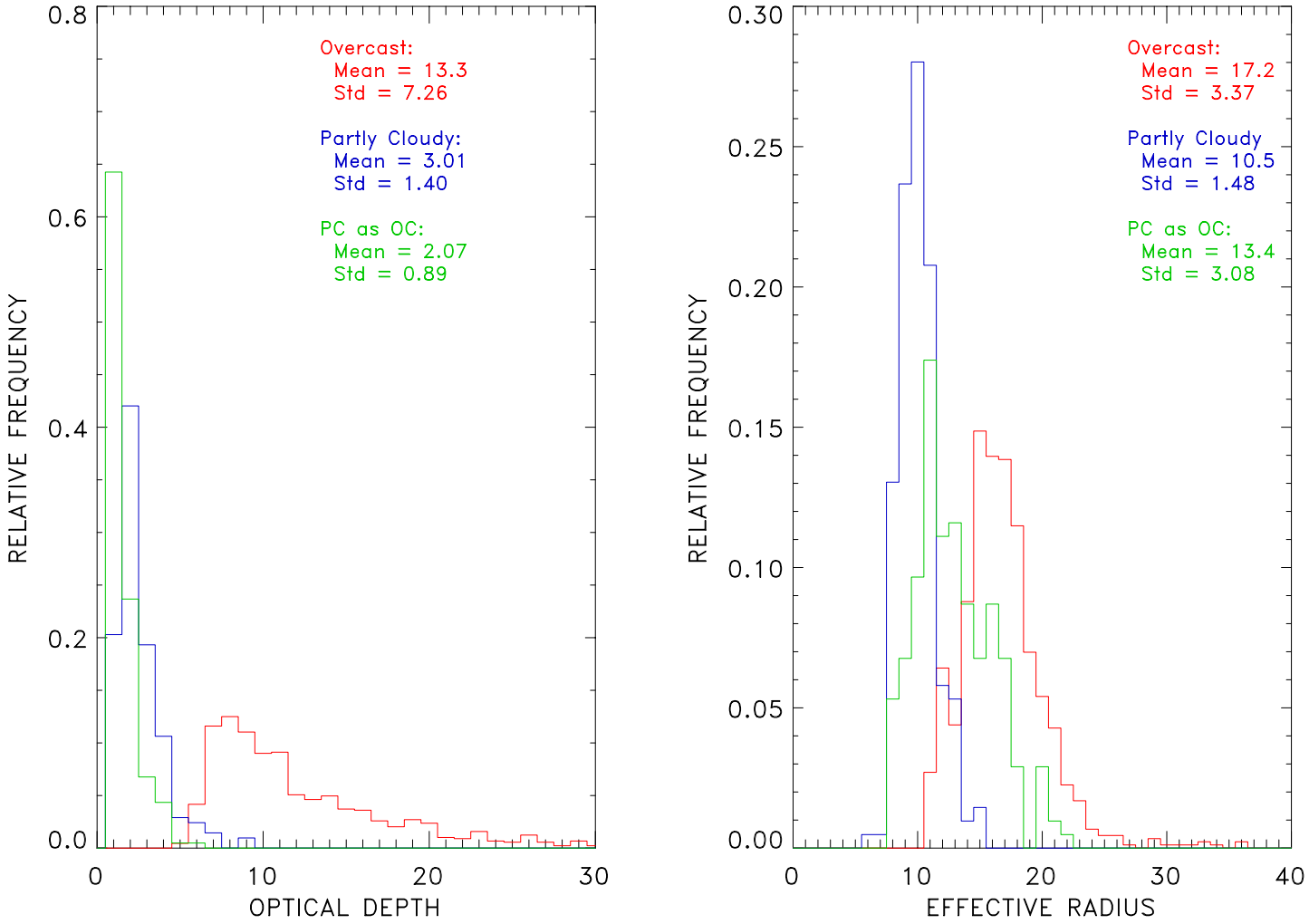

The distribution of retrieved optical depth and effective radius is shown for three populations in the subregion of 980212 19:03. Overcast retrievals (red) give larger values for optical depth and effective radius. Partly cloudy retrievals (blue) give smaller values. When partly cloudy pixels are retrieved as if they were overcast (green), slightly smaller optical depths are retrieved compared to the partly cloudy retrievals, and intermediate values of effective radii are retrieved compared to the partly cloudy and overcast distributions.

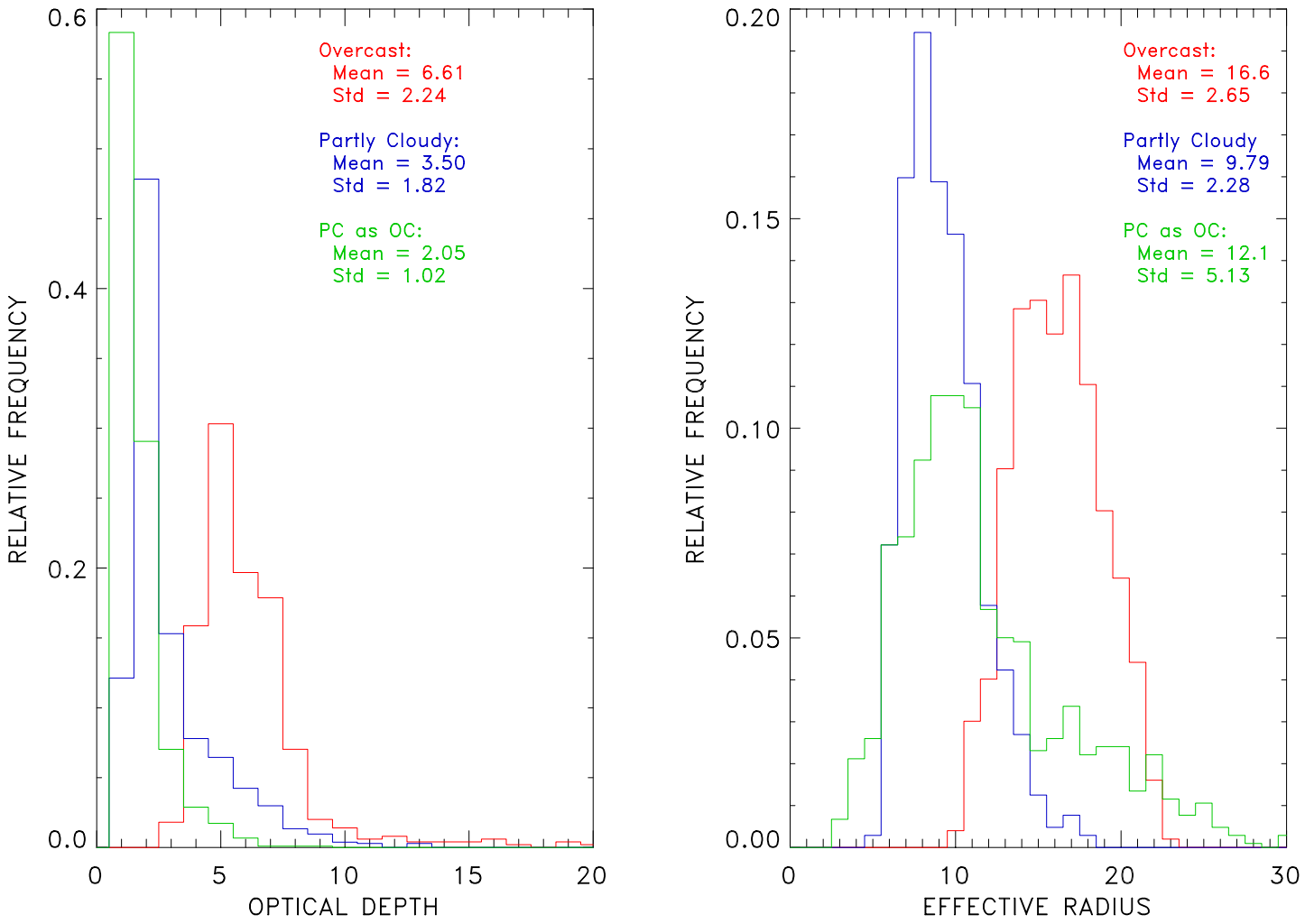

Same as previous figure, except the populations are drawn from a larger region of a different scene (980222 15:41). There is a wider distribution of cloud fraction for this subregion. The same relationships between the distributions are evident.

3. Aerosol direct radiative forcing from CERES/TRMM and AERONET data

By linking top of the atmosphere (TOA) radiative fluxes obtained by CERES/TRMM with surface measurements of aerosol optical depths obtained with the AERONET instrument at the Kaashidhoo Climate Observatory (KCO), Satheesh and Ramanathan (2000) derived emprical estimates of the direct aerosol radiative forcing for aerosols over KCO. The goal of this study is to extend the Satheesh and Ramanathan findings to other oceanic AERONET sites. The approach will use an aerosol model in combination with CERES broadband radiances and fluxes and AERONET optical depths. The aerosol model is used to extend the CERES estimates of the radiative fluxes to generate estimates of the diurnally averaged direct radiative forcing. The approach is to use the CERES broadband radiances to derive an aerosol optical depth, based on a given aerosol model, and use the retrieved optical depth to predict the diurnally averaged radiative forcing. Differences between model generated and CERES derived fluxes would be used to adjust the model estimated fluxes.

Estimates of aerosol burdens derived from satellite radiances are sensitive to the aerosol model used to link radiances with optical depths. For example, using CERES shortwave broadband bidirectional reflectances, optical depths derived for backscattered light and an average continental aerosol model differ by as much as 30% from those derived using the same shortwave reflectance and a tropical marine aerosol model. The aerosol models are described by Hess et al. (1998). The radiative forcing inferred from the reflected radiance, however, differ by only 8%. This reduction in difference results from the nearly identical anisotropic factors that relate radiances to radiative fluxes for the two aerosol models. Provided the predicted and observed

radiances match, the estimated radiative flux will be the same regardless of the aerosol model used to predict the radiances and fluxes.

Even though broadband radiances are used here to link shortwave radiances to radiative fluxes for ocean regions, the estimated fluxes appear to be insensitive to profiles of ozone and water vapor in the atmosphere. For a tropical marine aerosol, estimates of the radiative forcing obtained using tropical profiles of water vapor and ozone differ by 4% from those obtained using profiles for midlatitude winter conditions, for which the profiles of water vapor and ozone are markedly different.

SSF Edition 1 for TRMM (January – June, 1998) were analyzed to obtain shortwave radiances and fluxes, along with the collocated VIRS radiances, that fell within ± 50 km of an AERONET Site for which AERONET observations provided a surface measurement of optical depth within ± 1 hr of the TRMM overpass. The SSF observations were restricted to fields of view for which a retrieval of aerosol optical depth and radiative fluxes had also been performed. Few fields of view met these criteria. For Kaashidhoo, only 9 passes from the January – June, 1998 data satisfied these conditions and typically less than ten fields of view from these passes satisfied the conditions.

To verify that estimates of the TOA radiative forcing were relatively insensitive to the choice of the aerosol model, as theory predicts, calculations of shortwave, broadband reflectances (0.2–4 μm) were performed using optical depths retrieved using the CERES shortwave reflectances for the fields of view that met the analysis criteria. The optical depths were retrieved

using both the average continental and tropical marine aerosol models. The optical depths were then used to estimate the shortwave radiative fluxes. The calculated fluxes were within 2% of the observed shortwave fluxes, but there was a definite trend in the discrepancies with the retrieved optical depth. Also, calculations were performed assuming zero albedo for the ocean surface. The discrepancies are significantly worse when more realistic values are used for the ocean reflectance.

The optical depths used to predict the instantaneous shortwave fluxes were then used to estimate the diurnally averaged reflected shortwave fluxes, and these diurnally averaged fluxes were combined with the AERONET observations of optical depths to derive the diurnally averaged aerosol direct radiative forcing. For Kaashidhoo, the derived forcing was $-32\ Wm^{-2}$ per unit optical depth at 0.5 μm. This forcing is somewhat larger than the $-23\ Wm^{-2}$ reported by Satheesh and Ramanathan (2000). The number of observations that went into this estimate, however, is alarmingly small.

Optical depths retrieved using the broadband, shortwave reflectances were also compared with those obtained by AERONET. In addition, retrievals of optical depths were performed using the point spread function weighted VIRS 0.63-μm reflectance using the aerosol model adopted in the NOAA Phase-2 retrieval. The retrieved optical depths obtained using the SSF Edition 1 data agreed better with the AERONET observations than those obtained using the earlier SSF R4 data. The number of fields of view contributing to the R4 comparisons were much larger than those that contributed to the Edition 1 comparisons. Also, the optical depths derived using the NOAA

Phase-2 model differed markedly from both the AERONET observations and the optical depths reported on the SSF. Reasons for this discrepancy are being explored.

References

Coakley, J.A., Jr., and R. Davies, 1986: Effect of cloud sides on reflected solar radiation as deduced from satellite observations. *J. Atmos. Sci*., **43**, 1025-1035.

Hess, M., P. Koepke, and I. Schult, 1998: Optical properties of aerosols and clouds: The software package OPAC. *Bull. Amer. Meteor. Soc*. **79**, 831-844.

Satheesh, S.K. and V. Ramanathan, 2000: Large differences in tropical aerosol forcing at the top of the atmosphere and Earth's surface. *Nature*, **405**, 60-63.

AERONET AND CERES TRMM SSF COMPARISON SITES
JANUARY–AUGUST 1998

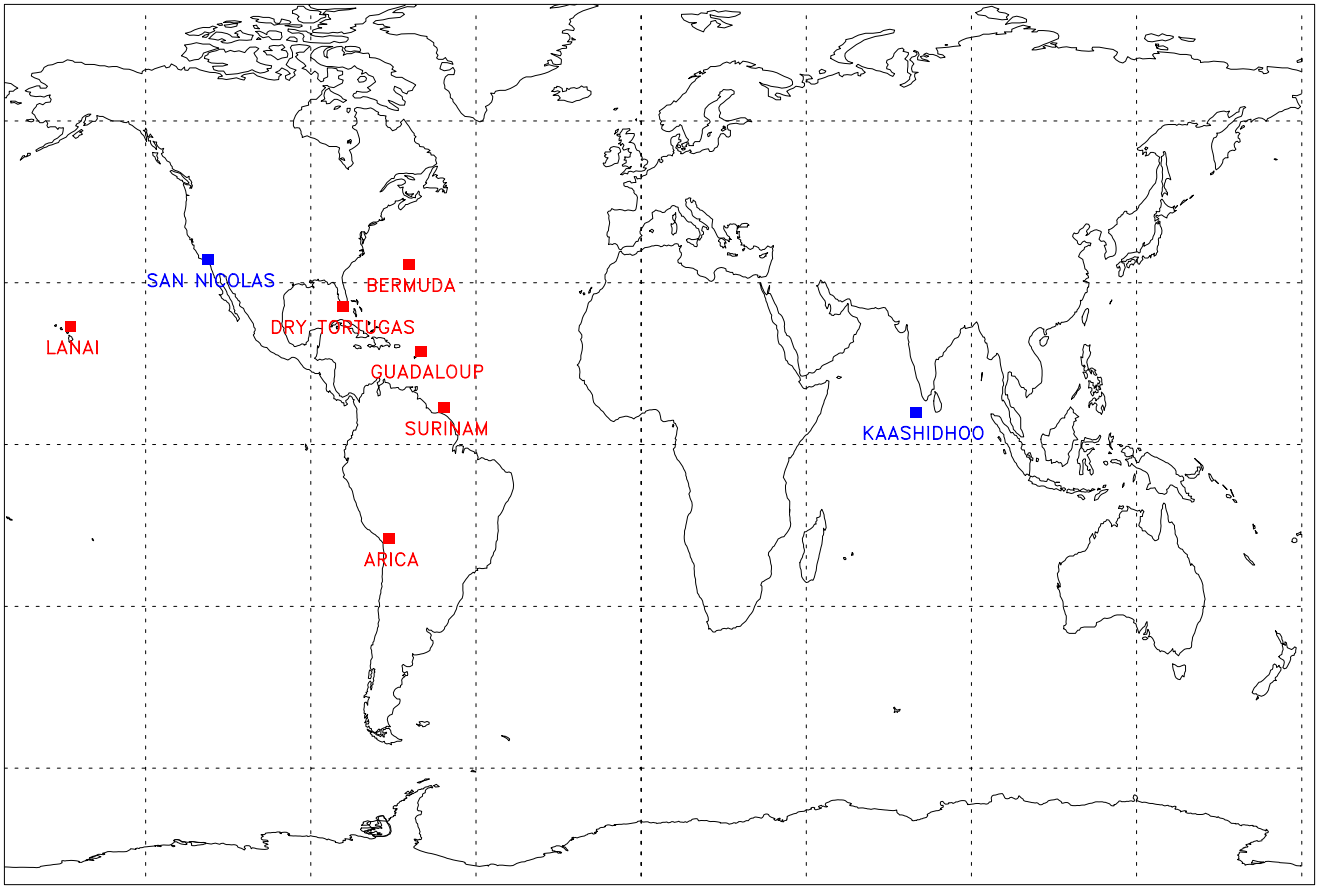

Figure 1. Sites for which collocated CERES TRMM observations and AERONET optical depths are potentially available. Sites in blue indicate matchups for R4.

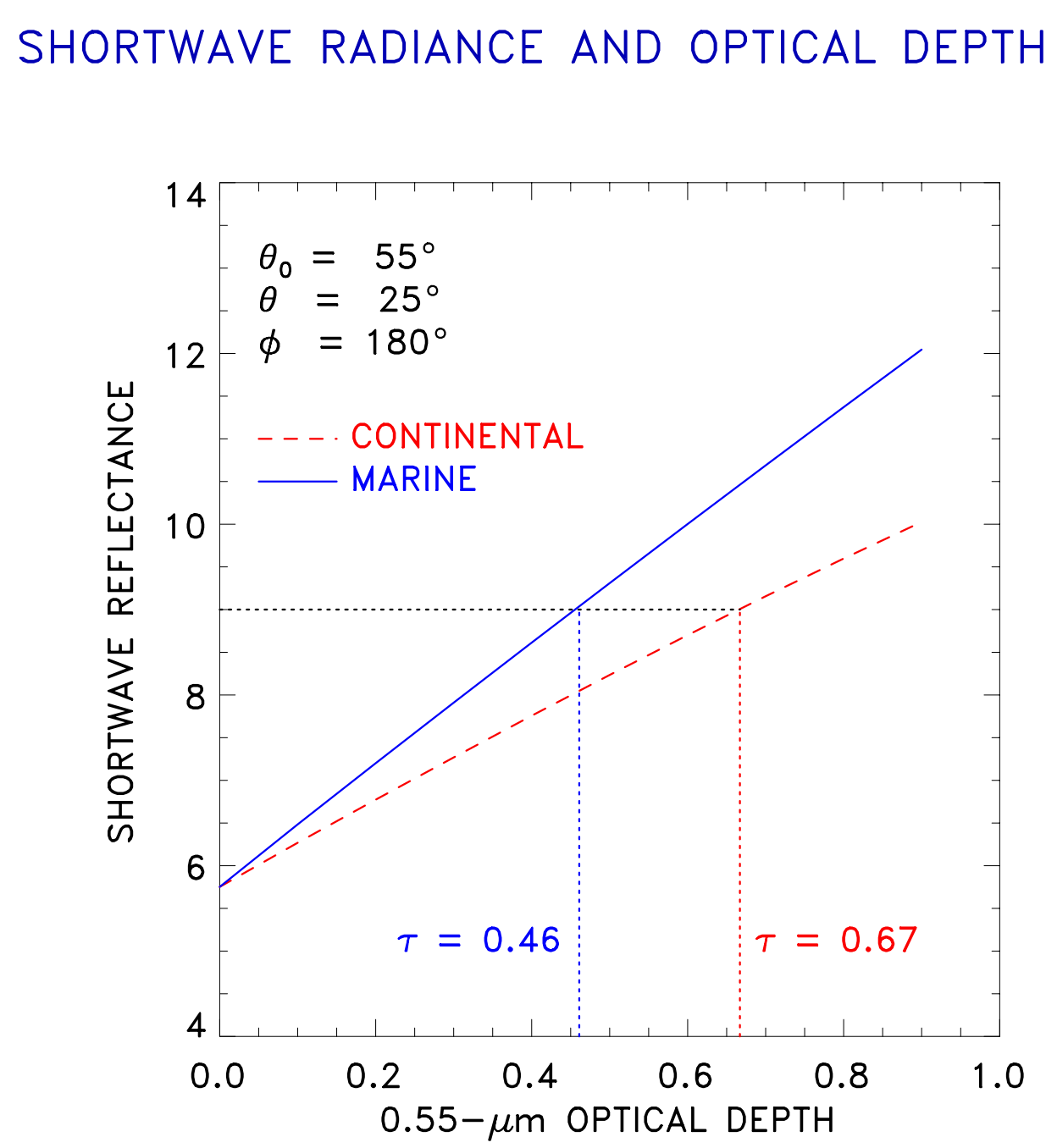

Figure 2. Broadband shortwave bidirectional reflectance and 0.55-μm optical depth.

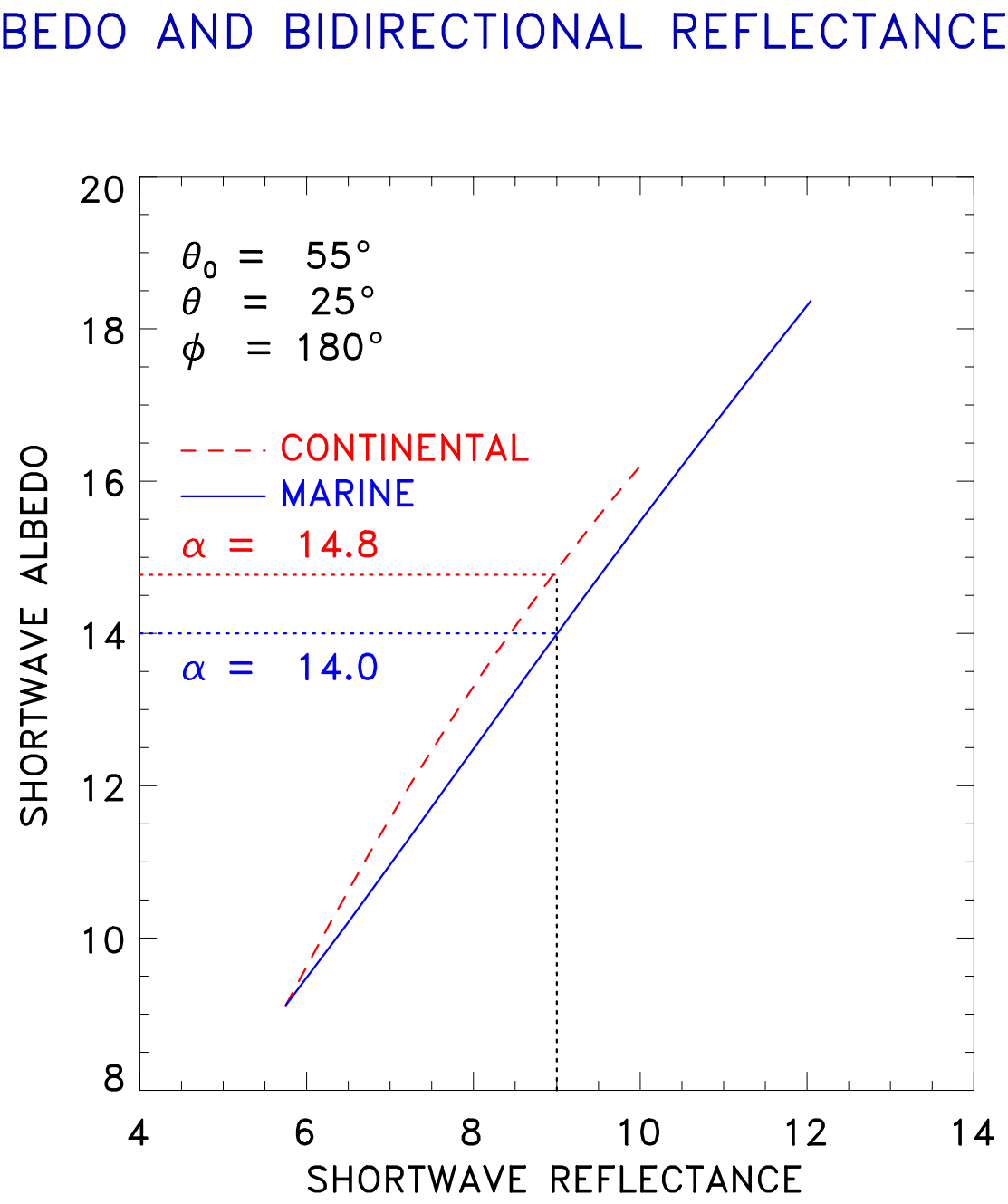

Figure 3. Broadband albedo and broadband shortwave bidirectional reflectance.

DIFFERENCES IN WATER VAPOR AND OZONE

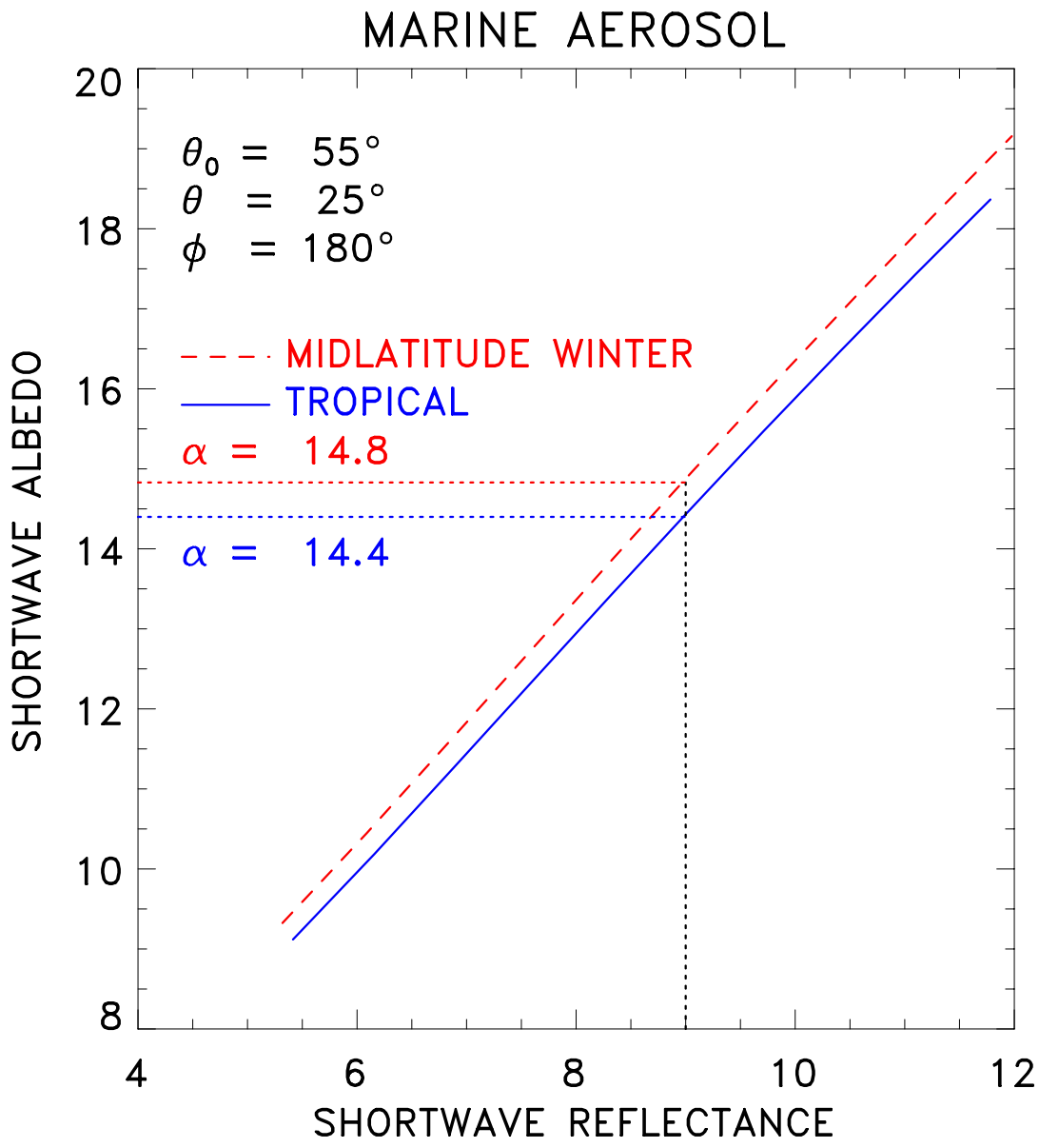

Figure 4. Broadband albedo and broadband shortwave bidirectional reflectance calculated for tropical and midlatitude winter climatological profiles of water vapor and ozone.

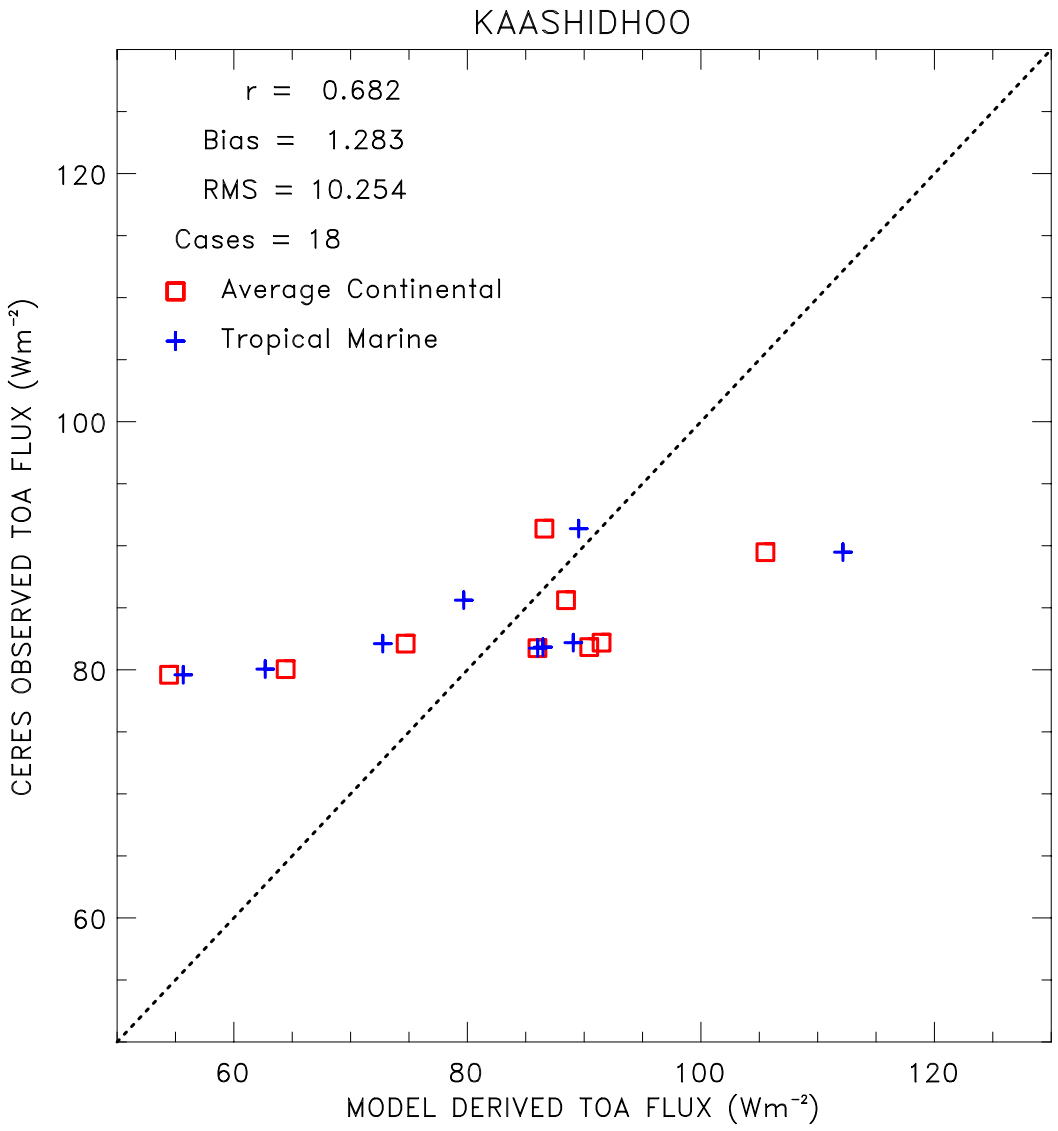

Figure 5. Observed and calculated shortwave radiative fluxes for Kaashidhoo. Observations are from SSF Edition 1 for January – June 1998.

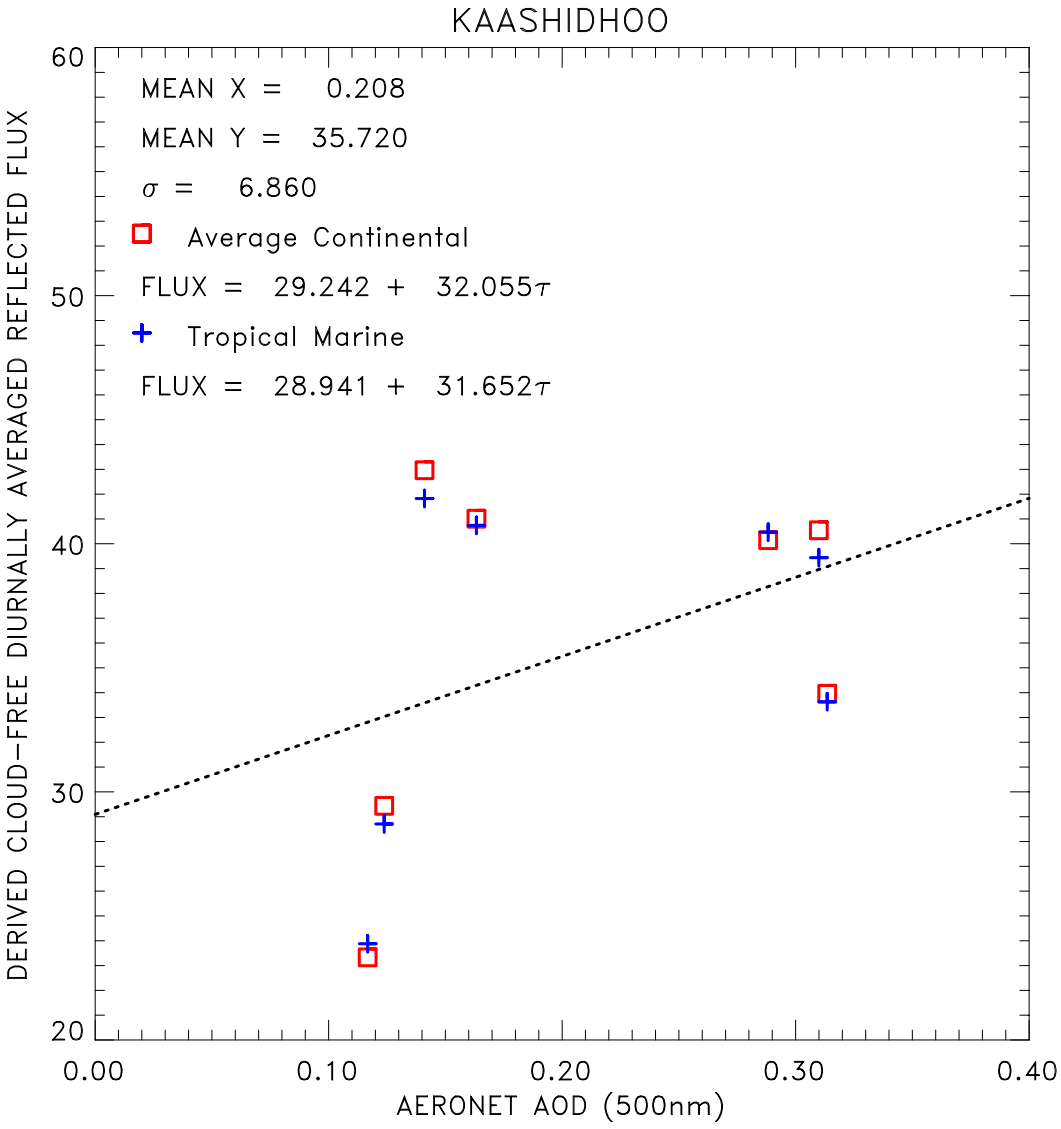

Figure 6. Diurnally averaged radiative fluxes (Wm^{-2}) and AERONET 500nm optical depth for Kaashidhoo.

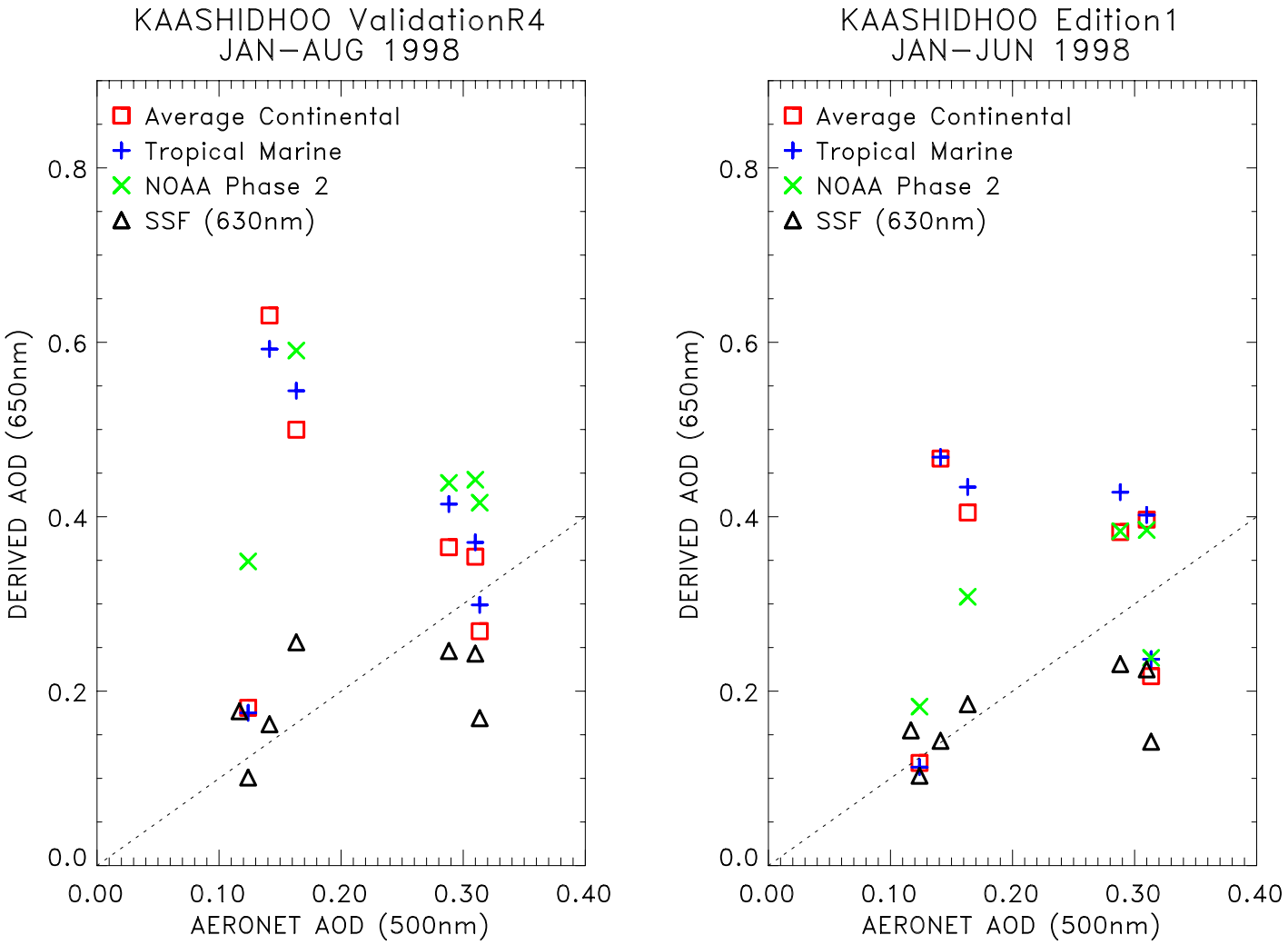

Figure 7. Retrieved and observed optical depths for Kaashidhoo. Observations are from the SSF R4 and SSF Edition 1.